

Mechanisms of power augmentation in two side-by-side vertical axis wind turbines

Aaron S. Alexander^{a,*}, Arvind Santhanakrishnan^b

^a*Mechanical Engineering Technology, Department of Engineering Technology, Oklahoma State University, Stillwater, OK 74078*

^b*Department of Mechanical and Aerospace Engineering, Oklahoma State University, Stillwater, OK 74078*

Abstract

Using two-dimensional computational fluid dynamics (CFD) simulations, this study examines the physical mechanisms of performance improvement in a double rotor vertical axis wind turbine (VAWT) as compared to a single rotor VAWT. A power coefficient (C_P) improvement of around 10% was observed in the double rotor VAWT. It was found that this is primarily due to a reduction in the bypass flow around the outside of the single rotor VAWT. The single rotor VAWT is shown to cause greater than 54% of the incoming flow to bypass around the outside of the VAWT. By placing a second rotor in the system, the cross-stream flow that would normally exist to one side is suppressed due to the opposing cross-stream flow from the second rotor. The collision of cross-stream velocities results in a high pressure field upstream of the rotors. This high pressure field re-directs more flow through the rotors, reducing the total bypass down to below 51%. This reduction in total bypass is solely due to the reduction in bypass on the interior of the double rotor system as the exterior side actually experiences an increase in bypass of about 83%.

Keywords: CFD; VAWT; Darrieus; Wind turbine array; Wind power

1. Introduction

- 1 In 2011, Dabiri published a paper demonstrating that closely spaced arrays of
- 2 vertical axis wind turbines (VAWT) can increase the power density of wind farms
- 3 by 6-9 times that of current horizontal axis wind turbine (HAWT) farms [12].
- 4 Using field measurements of the three-bladed 1.2kW Windspire VAWT [3, 26,
- 5 20], Dabiri found that placing side-by-side counter-rotating turbines separated
- 6 by 1.6 rotor diameters gave an increase in power output in the range of 10% when
- 7 the wind is perpendicular to the two turbines [12] as shown in Figure 1a and b.

*Corresponding author

Email address: aaron.s.alexander@okstate.edu (Aaron S. Alexander)

URL: <http://www.appliedfluidslab.org/> (Arvind Santhanakrishnan)

8 The power output varies as the wind direction changes, but for many conditions
 9 the power augmentation remains [12, 28]. Additionally, it has been shown that
 10 the turbine pair have a wake recovery to 95% of the free stream velocity within
 11 six rotor diameters which, while worse than the typical four diameters of a single
 12 VAWT, is still better than the fifteen diameters required by a single HAWT [19].
 13 This means that proper placement of downstream turbines can result in a higher
 14 density of VAWTs relative to a HAWT wind farm and thus an increase in power
 15 output per land area [1, 7, 11, 27, 10]. In order to understand and optimize
 16 this performance increase, a better understanding of the flow physics needs to
 17 be developed.
 18 Giorgetti et al. used two-dimensional computational fluid dynamics (CFD) sim-
 19 ulations to model counter-rotating VAWT pairs [17]. They found performance
 20 improvements in both the counter-down (Figure 1a) and counter-up (Figure
 21 1b) configurations which They attribute to the acceleration of flow between the
 22 two turbines re-energizing the wake. Zanforlin and Nishino followed up on this
 23 work by running a comprehensive set of 2D CFD simulations on double ro-
 24 tors VAWT systems varying the gap spacing, tip-speed ratios (TSR), and wind
 25 directions [28]. This study further confirmed the power augmentation effect
 26 and showed similar, though not perfect, agreement with the measurements of
 27 Dabiri's group [7] concerning power output with changing wind incidence an-
 28 gles. They attributed the improvement in power output to (1) a contraction in
 29 downstream wake and (2) the improved orientation of incoming flow for lift gen-
 30 eration. Both changes are attributed to the reduction of cross-stream velocity
 31 between the turbines due to opposing velocity direction as the flow is squeezed
 32 between the two VAWTs.

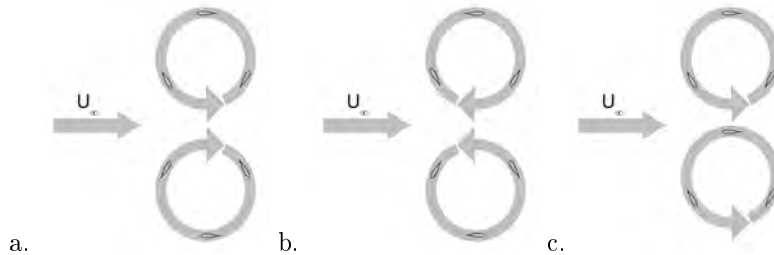


Figure 1: Rotor rotation with respect to the free stream. (a) Counter-down: Counter-rotating rotors rotate downstream as they come together. (b) Counter-up: Counter-rotating rotors rotate upstream as they come together. (c) Co-rotating: Co-rotating rotors rotate in the same direction.

33

34 Bremseth and Duraisamy [6] modeled two bladed pairs and columns of co-
 35 ounter-rotating VAWTs. They examined the velocity field through the
 36 turbine array and found a similar velocity speedup between the rotors to that
 37 found by Zanforlin and Nishino [28]. Chen et al. analyzed a larger three-airfoil
 38 double rotor system where they varied the TSR, wind direction, and blade angle

39 for their simulations [9]. They found, in the best case, a 10% improvement
40 in power output. Lam and Peng [21] conducted wind tunnel measurements
41 of the wake of both co-rotating (Figure 1c) and counter-rotating (Figures 1a
42 and b) double rotor systems with five airfoils. They were able to measure
43 streamwise, vertical, and cross-stream velocities starting at one diameter and
44 continuing to 10 diameters downstream. In the near field, they found velocities
45 deficits behind each turbine to be around 75%, although the wake recovery
46 they found was slower than showed by Dabiri's in-situ measurements. This is
47 likely due to the more ordered nature of the wind tunnel flow versus the higher
48 turbulence found in nature. It should be noted that these previous studies
49 have not examined the time-varying pressure field between the two rotors in the
50 double rotor configuration.

51 In all, the previous works demonstrate agreement on two main coarse mecha-
52 nisms for the power increase. First, in the double rotor system, the blockage
53 results in straight streamwise velocity in between the adjacent turbines due to
54 cancellation of opposing y-velocities [15, 28]. Second, the wake behind each
55 adjacent turbine is significantly contracted from the wake of a single turbine
56 [15, 28]. Each of these mechanisms is certainly a part of the power increase and
57 examining the flow physics at a finer level reveals that each is connected by the
58 pressure field created in the double rotor system.

59 Using 2D unsteady Reynolds Average Navier Stokes (URANS) CFD simulations,
60 the current study quantifies and reinforces each of those coarse mechanisms
61 while examining the performance increase mechanisms in finer detail down to
62 the airfoil level. Specifically, this study asks: how do the fluid mechanics differ
63 between the single and double rotor systems and what is driving the additional
64 power generation?

65 There are several limitations in the following simulations that should be noted.
66 First, since the simulations are two-dimensional there are no three-dimensional
67 effects. This means reduced turbulent mixing and a delayed wake recovery
68 since flow can only enter from the wake sides and not from the airflow above the
69 VAWTs. Additionally, since the purpose of this study is to examine the physical
70 mechanisms of power augmentation, there was no effort made to vary the gaps,
71 wind direction, or TSR. Instead, this study focuses on the fluid mechanics that is
72 driving the power generation differences. Finally, these simulations are missing
73 many of the secondary losses that would typically occur in a VAWT system such
74 drag on struts [8], interference of the center column, power conversion losses,
75 etc.

76 **Nomenclature**

77 A - area

78 C_P - power coefficient

79 D - rotor diameter, 1.2 m

80 E - energy

- 81 H - rotor height, 6.3 m
- 82 P - power
- 83 Q - volumetric flow
- 84 R - rotor radius, 0.6 m
- 85 r - radial distance from the rotor axis
- 86 T - torque
- 87 TSR - tip speed ratio, 2.3
- 88 U - local velocity magnitude
- 89 \bar{U} - surface average of velocity magnitude
- 90 U_∞ - wind velocity, 8 m/s
- 91 Z - position in rotor cycle as a fraction of a complete cycle
- 92 C_T - coefficient of force in the radial direction
- 93 F_T - force in the radial direction
- 94 $P_\%$ - percentage increase in power
- 95 \hat{V} - volume
- 96 $\hat{V}_\%$ - percentage increase in volume
- 97 u - local velocity parallel to the streamwise direction
- 98 u_r - radial velocity with respect to the Rotor axis
- 99 v - local velocity in the cross-stream direction
- 100 x - distance from rotor center parallel to the streamwise direction
- 101 y - distance from rotor center perpendicular to the streamwise direction
- 102 t - airfoil max thickness, 0.025 m
- 103 w - wake width
- 104 ω - angular velocity, $\frac{TSR \times U_\infty}{R}$
- 105 ρ - air density
- 106 θ - angular position

107 2. Model Parameters and Methods

108 2.1. VAWT System

109 Since the 1.2 kW Windspire has served as a test bed for previous studies
 110 [1, 3, 7, 11, 12, 13, 17, 19, 27, 28], it was adopted for this study as well. The
 111 three-bladed Windspire uses a DU06W200 airfoil with a chord length of 0.127
 112 m, a rotor diameter of 1.2 m, a maximum thickness of 0.025 m, and a rotor
 113 span of 6.1 m [28]. The TSR was set at a constant 2.3 and the center-to-center
 114 distance of the adjacent rotors was set at 1.8 m. The rotor side with the gap
 115 between the two rotors is referred to as the adjacent side while the opposite
 116 rotor side is referred to as the non-adjacent side (Figure 2). The wind speed
 117 was maintained at a constant 8 m/s. At that wind speed, the Windspire turbine
 118 has a field measured power coefficient (Eq. 4) of 0.18 [18]. Figure 2 shows the
 119 layout of the double rotor system as well as the convention for cycle position
 120 as used in this study. Since the two rotors in the double rotor system are part
 121 of a symmetric system, the output of either rotor is deemed interchangeable
 122 with any minor deviations due to small differences in the distribution of the
 123 unstructured mesh leading to altered turbulence. Any full rotor values given
 124 are an average of the upper and lower rotors.

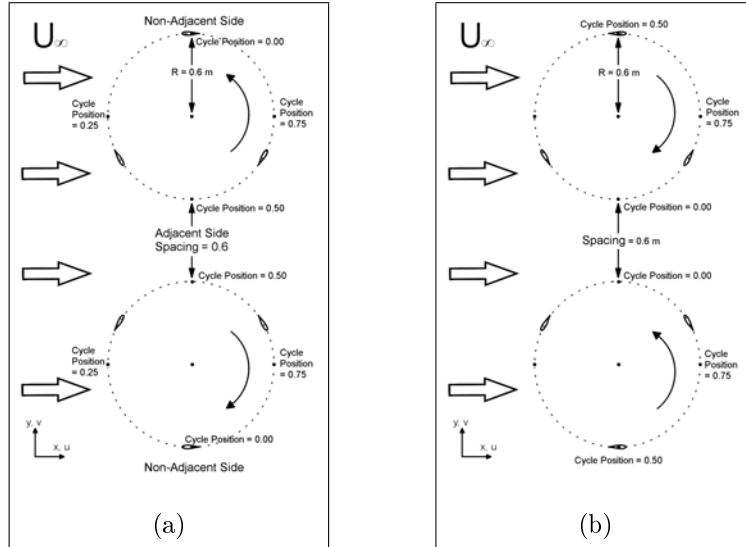


Figure 2: Rotor system layout. (a) counter-down (b) counter-up

125 2.2. Computational Methods

126 2.2.1. CFD Setup

127 The simulations completed for this study used Siemens' commercial CFD
 128 code Star-CCM+ [25] with an unsteady, two-dimensional (2D), low- y^+ , implicit
 129 segregated $k - \omega$ Reynolds Averaged Navier-Stokes model. Each simulation

utilized about 15,000 processor hours to complete. In order to calculate the power production, the torque, T , for a single cycle was cycle-averaged by:

$$T_{avg} = \frac{1}{2\pi} \int_0^{2\pi} T d\theta \quad (1)$$

where θ is the angle in the cycle. The torque, T , is given by:

$$T = F_T R = \frac{1}{2} C_T \rho A R V^2 \quad (2)$$

where R is the rotor radius, C_T is the coefficient of force in the radial direction, ρ is the air density, A is the planform area of the airfoil, and V is the local velocity impinging on the airfoil. Using the average torque, power, P , can be calculated by:

$$P = \omega T_{avg} \quad (3)$$

where ω is the angular velocity. The average power per cycle was used to calculate the power coefficient, C_P :

$$C_P = \frac{P}{0.5 \rho D H U_\infty^3} \quad (4)$$

where ρ is the air density, D is the rotor diameter, H is the rotor height, and U_∞ is the wind velocity.

For VAWT CFD simulations, Balduzzi et al. recommend a minimum domain of 60D wide, 40D upstream of the rotor, and 100D downstream of the rotor where D is the VAWT rotor diameter [2]. The present study found the best results with a domain size of 60D wide, 60D upstream of the rotor, and 143D downstream of the rotor as shown in Figure 3. The inlet boundary conditions are set at the wind speed velocity with turbulent viscosity ratio and turbulence intensity values set to 10 and 0.1, respectively, as recommended by both Lanzafame et al. [22] and Daroczy et al. [14].

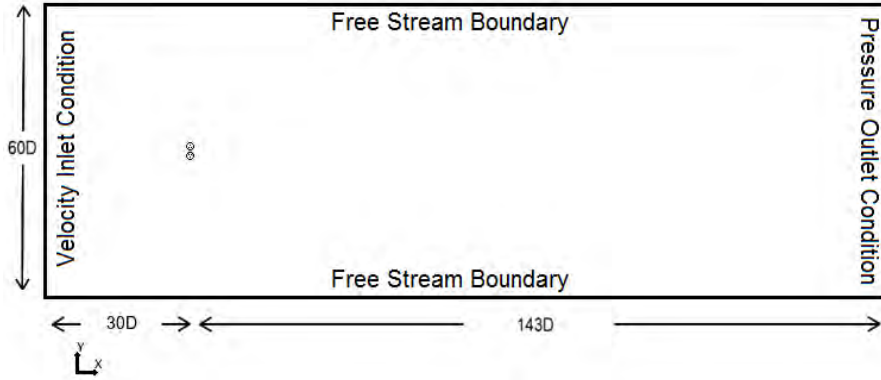


Figure 3: Domain geometry used for CFD simulations. Boundary conditions are labeled. D = rotor diameter = 1.2 m, U_∞ = velocity at inlet = 8 m/s.

149 The outlet boundary is set at ambient pressure. The side wall boundary
 150 condition is set up as a free stream condition in most of the simulations where
 151 the velocity, turbulent viscosity ratio, and turbulence intensity are maintained
 152 at the same values as the inlet. The free stream condition is especially helpful
 153 as it is formulated to allow flow to enter and leave the domain. This ensures
 154 that the VAWTs do not have a local speedup due to side-wall flow channeling,
 155 a concern demonstrated by Bianchini et al. [5]. Also, since the flow can leave,
 156 pressure reflections are minimized, allowing for a more accurate depiction of
 157 the local pressure field around the rotor and airfoils. This is an advantage as
 158 pressure fields can often be difficult to properly model in a two-dimensional CFD
 159 study when using wall boundaries as pressure reflection from the boundaries can
 160 subsume the smaller pressure variations in the actual system.

161 As a point of comparison, each simulation was also completed with a slip
 162 sidewall boundary condition. The slip boundary wall does not allow flow to enter
 163 or leave. These simulations were used to verify the bypass flow that passes to
 164 the side of the rotors which, in order to be accurate, requires preventing flow
 165 from entering/leaving the side boundaries.

166 The mesh domain had 576 nodes along each airfoil (Figure 4), 102,000 poly-
 167 hedral elements in an overset mesh arrangement are used to model each rotor,
 168 with 462,000 and 588,000 total elements for the single and double rotor systems
 169 respectively. The rotating domain had a diameter of 1.68 m so it extends 0.24
 170 m past the diameter of the rotor (Figure 5).

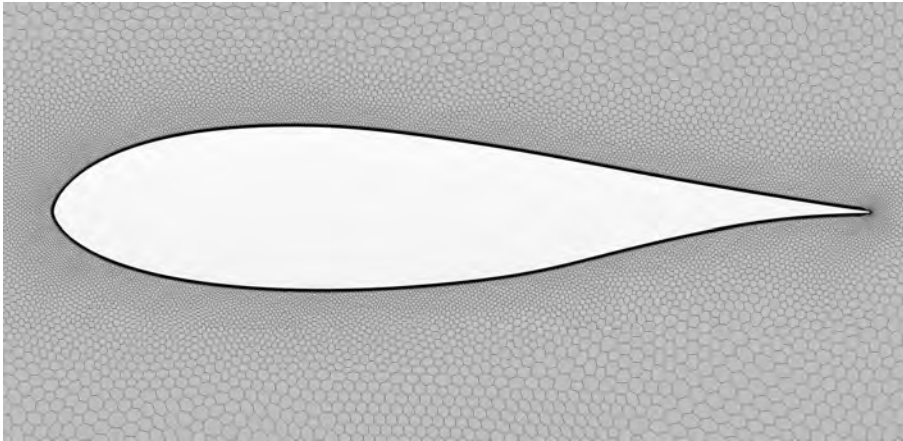


Figure 4: Mesh around a single airfoil

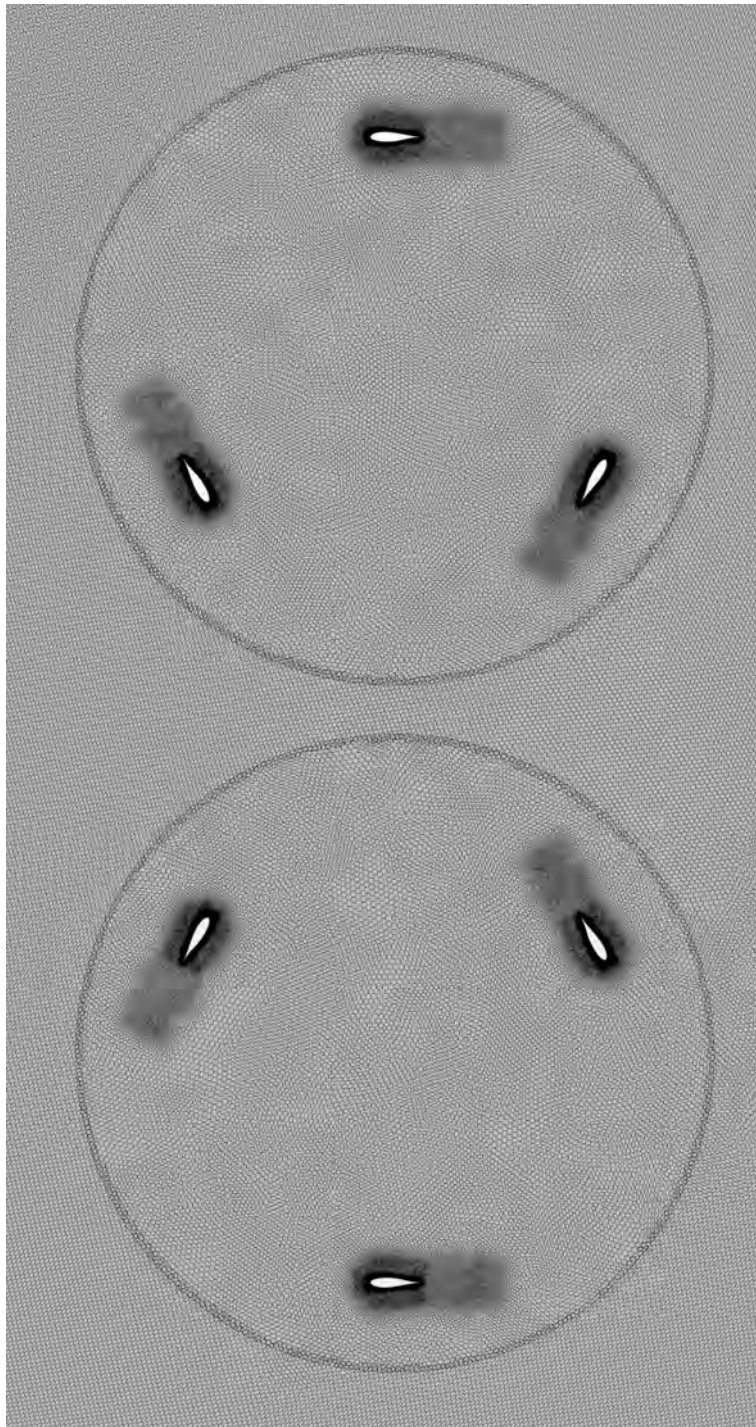


Figure 5: Mesh used for double rotor system

171 Each airfoil used a mesh wake refinement setting that allowed the mesh to
 172 gradually increase in size as it progressed away from the airfoil. The boundary
 173 layer on the airfoils are captured using 30 prism layers with a total thickness
 174 of 0.43 mm. The first prism layer was maintained at $5 \mu\text{m}$ so that the wall y^+
 175 values stays well below 0.9.

176 After running dozens of preliminary simulations, it was found that the power
 177 coefficient settled to a steady-state value in the range of 20 to 26 rotations of
 178 the rotor. In order to ensure convergence, each of the final simulations were
 179 run to 30 cycles before flow field data collection began. The data collection
 180 continued for three cycles with the entire velocity, vorticity, and pressure fields
 181 outputted every 1/64th of a cycle. Since the time to complete a single cycle
 182 is determined by the TSR and wind speed, it can be shown that the total
 183 simulation time needed to complete 33 cycles is 6.76 s. The time step used
 184 was variable based on the current maximum Courant number in the domain,
 185 thus any values given here are representative values rather than exact. The
 186 maximum Courant number for any given time step was actually only present in
 187 a few cells.

188 In order to get the flow field set up, the simulations were initialized with large
 189 time steps that are progressively reduced until the maximum Courant number
 190 is maintained at one or below for the final three cycles as shown in Table 1. The
 191 angular rotation per time step is well below the maximum of 1° recommended
 192 by Castelli et al. [8] and drops below the 0.1° used by Rezaeiha et al. [23] while
 193 the progressive decrease in time step is as recommended by Ghasemian et al.
 194 [16].

Max Courant #	Avg Courant #	Cycle Range	Time Step (s)	Angular Rotation
80	0.65	0-10	1.00×10^{-4}	0.176°
10	0.13	10-25	1.90×10^{-5}	0.033°
8	0.10	25-27	1.46×10^{-5}	0.026°
4	0.05	27-30	7.40×10^{-6}	0.013°
1	0.01	30-33	1.79×10^{-6}	0.003°

Table 1: Approximate time step and angular movement for a given maximum domain Courant number.

195 2.2.2. Mesh Validation

196 The simulations in this study are deemed to be converged when the power
 197 coefficient has settled to a steady-state value. A mesh independence study
 198 has been completed comparing the resultant C_P of the base mesh with the
 199 C_P when the mesh base size has been reduced by 10% and 20%. These mesh
 200 reductions result in an increase in the double rotor system from 588,000 elements
 201 to 701,000 and 859,000 elements, respectively. The counter-down double rotor
 202 system shows a C_P of 0.397 for the base mesh. The mesh independence studies
 203 showed no change in that value.

204 2.2.3. Calculation Methods

205 The previous studies have consistently discussed qualitative differences in the
 206 rotor wakes between the single and double rotor VAWTs so this study sought
 207 to expand the analysis by quantifying the difference in wake width. In order
 208 to make the quantification, the rotor wake width is defined as the cross-stream
 209 distance between points that are 95% of the free stream velocity.

210 This study also sought to calculate the flow entering the rotor domain, but
 211 finding the total flow entering the VAWT can be difficult as the airfoils are
 212 constantly changing both the direction and speed of the local flows. If the
 213 measurement plane is placed directly upstream of the rotor the measured flow
 214 will be over-predicted as flow can still be pushed to the outside of the airfoils
 215 once it passes through the plane. If the measurement plane is placed inside
 216 the rotor then the signal over time is corrupted as the airfoils pass through
 217 the plane resulting in reversed flows and blockage effects. If the measurement
 218 plane is placed downstream in the wake then assumptions need to be made
 219 about the width as the slowing flow spreads out into a greater area. Thus, it
 220 is better to infer the flow through the rotor by measuring the total volume of
 221 air, $\hat{V}_{side\ bypass}$, that passes around the outside of the rotor over a given number
 222 of cycles. That value can be compared to the total volume, $\hat{V}_{freestream\ to\ side}$,
 223 that passes through the same area in the absence of the rotors. It is necessary
 224 to measure the total volume of air over a given number of complete cycles
 225 because the 3 times per cycle proximity of an airfoil causes spikes in the bypass
 226 flow. By using total volume of passing air, these spikes are accounted for in the
 227 calculation. The total volume of air, \hat{V}_{rotor} , that passes through the rotor for a
 228 given time period is:

$$\hat{V}_{rotor} = \hat{V}_{side\ bypass} - \hat{V}_{freestream\ to\ side} \quad (5)$$

229 with the bypass ratio calculated by:

$$\% bypass = \left(1 - \frac{\hat{V}_{rotor}}{\hat{V}_{freestream\ through\ rotor\ area}} \right) \times 100\% \quad (6)$$

230 and the increase in volume, $\hat{V}_{\%}$, through the rotor is given by:

$$\hat{V}_{\%} = \left(\frac{\hat{V}_{double\ rotor} - \hat{V}_{single\ rotor}}{\hat{V}_{single\ rotor}} \right) \times 100\% \quad (7)$$

231 To quantify the approximate power generation percent increase, $P_{\%}$, for a
 232 given change in total volume passing through the rotors, Equations 1, 2, and 3
 233 are combined to give:

$$P_{\%} = \frac{P_{double\ rotor} - P_{single\ rotor}}{P_{single\ rotor}} \times 100\% = \left[\left(\frac{\hat{V}_{\%}}{100\%} \right)^2 + \frac{2\hat{V}_{\%}}{100\%} \right] \times 100\% \quad (8)$$

234 3. Results and Analysis

235 3.1. Power Coefficient

236 The single rotor simulations for this study show a power coefficient, C_P , of
 237 0.360. This is higher than the actual field measured electrical output mentioned
 238 above of 0.18, but this difference is to be expected as this study only models
 239 the aerodynamic aspects of the rotor and neglects any of the secondary losses
 240 mentioned in the introduction. When put into the double rotor configuration,
 241 the power coefficient increased to an average of 0.397 for the counter-down ar-
 242 rangement and 0.408 for the counter-up arrangement. The percentage increases,
 243 calculated by:

$$\% \text{Improvement} = |C_{P,\text{double rotor}} - C_{P,\text{single rotor}}| / C_{P,\text{single rotor}} \quad (9)$$

244 of 10.1% and 13.2%, respectively, over the single rotor is comparable to that
 245 found by previous researchers [7, 15, 28].

246 Figure 6 shows the three cycle phase averaged C_P of a single airfoil in the
 247 single and double rotor configurations with respect to the cycle position. The
 248 four regions in Figure 6, labeled A, B, C, and D, depict sections of the cycle
 249 where the output clearly favors either the single or double rotor configuration.

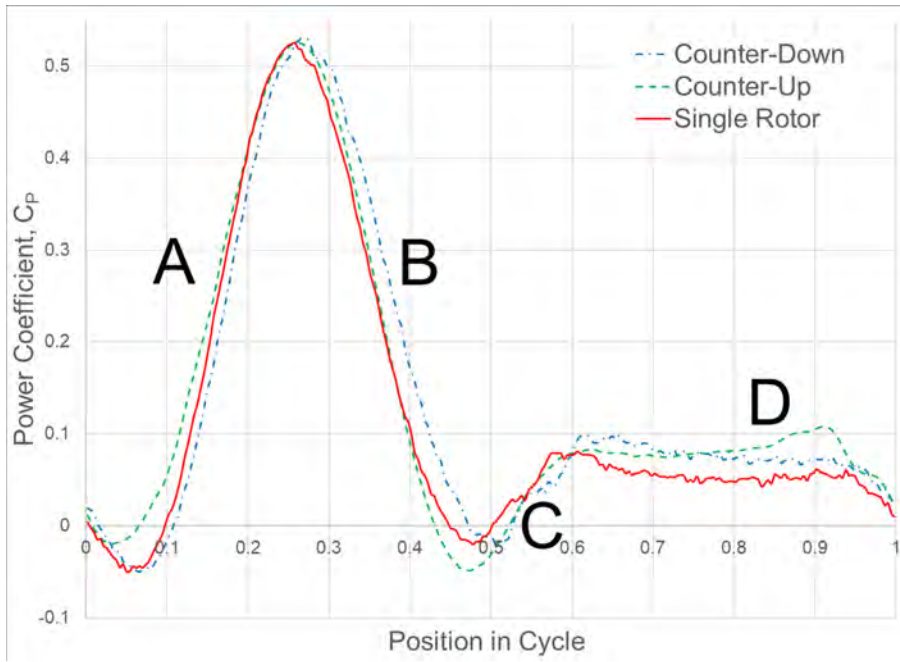


Figure 6: Three cycle phase averaged power coefficient of a single airfoil versus position in the cycle. Section A spans 0.14 to 0.29, Section B spans 0.29 to 0.46, Section C spans 0.46 to 0.60, Section D spans 0.60 back around to 0.14.

250 The total energy for each section is compared between the single and double
 251 rotor systems by integrating C_P over that section then calculating the percent
 252 difference between systems by:

$$\% \text{ gain/loss between systems} = \frac{\int_{\text{section}} C_{P,2Rotor} dZ - \int_{\text{section}} C_{P,1Rotor} dZ}{\int_{\text{section}} C_{P,1Rotor} dZ} \times 100\% \quad (10)$$

253 The relative performance between sections is given by:

$$\% \text{ of full cycle power} = \frac{\int_{\text{section}} C_P dZ}{\int_{\text{fullcycle}} C_P dZ} \times 100\% \quad (11)$$

254 3.1.1. Counter-down Airfoil Analysis

255 Section A shows the single rotor airfoil output shadowing slightly above the
 256 counter-down double rotor output as the cycle goes from $Z = 0.14$ to 0.29 .
 257 Section B starts where the curves cross at the end of Section A and continues to
 258 $Z = 0.46$. It is important to note that, although Sections A and B are of similar
 259 duration, Section B produces more power for the double rotor than it loses
 260 through Section A. In fact, while the double rotor system loses 6.76% relative
 261 to the single rotor through Section A, it improves by 27.56% through Section B.
 262 The two curves cross again at the start of Section C which proceeds from the end
 263 of Section B through $Z = 0.60$. This section represents a significant reduction in
 264 power production by the double rotor system of 35.29% below the single rotor
 265 system. Yet, as shown in Table 2, the power production for the single rotor
 266 in this region represents less than 3% of the total power production over a full
 267 cycle so a difference at this point means very little. Section D represents most
 268 of the downstream side of the rotor as it covers $Z = 0.6$ back around to $Z =$
 269 0.14 . This is an important region as the increase is 57.47% above the single
 270 rotor driving up the percentage of power production to over 1/5th the total
 271 power production.

Cycle Section	% of Total Power Production Equation 11		
	Single Rotor	Counter-up	Counter-down
Section A	47.89%	43.93%	40.25%
Section B	31.96%	28.60%	36.75%
Section C	2.89%	0.76%	1.68%
Section D	17.26%	26.70%	21.32%

Table 2: Power produced in each of the cycle regions shown as A,B,C, and D in Figure 6. Total improvement is 10.1%.

272 3.1.2. Counter-up Airfoil Analysis

273 The counter-up double rotor produces more power through Section A than
 274 either the single rotor or the counter-down double rotor, yet it then dips well

275 below both at the end of Section B and into Section C. Table 3 shows that
 276 the counter-up gets most of its advantage over the single rotor in Section D on
 277 the downstream of the rotor cycle where it more than doubles the single rotor
 278 output.

Cycle Section	Gain/Loss Over Single Rotor Equation 10	
	Counter-up	Counter-down
Section A	2.84%	-6.76%
Section B	0.34%	27.56%
Section C	-70.36%	-35.29%
Section D	104.65%	52.80%

Table 3: C_P comparison between single and double rotor systems in each of the cycle regions shown as A,B,C, and D in Figure 6.

279 3.2. Rotor Wake

280 As mentioned previously, the cited literature consistently agree that the
 281 two rotor system resulted in a narrower wake per rotor than the single rotor
 282 system, however, the actual wake width was not quantified [15, 28]. It should
 283 be reiterated that, since this is a two-dimensional simulation, the wake recovery
 284 does not include any effect of momentum transfer between the free stream layer
 285 above the VAWTs. It does include momentum transfer with the free stream
 286 to the sides since the side boundaries maintain a constant velocity, but even
 287 this momentum transfer is reduced since two-dimensional models lack the full
 288 turbulent mixing present in three-dimensions.

289 Even so, a comparison between the two-dimensional results gives a general
 290 understanding of the relative impact on the flow field. Figure 7 shows the nor-
 291 malized wake widths behind the single and double rotor systems. The flow
 292 between the double rotors, constrained from expanding freely, instantly cre-
 293 ates a thinner wake than the single system. This dichotomy becomes more
 294 pronounced as the distance downstream is increased until, at just about 8 di-
 295 ameters downstream (Figure 8), the single rotor wake loses coherence breaking
 296 up into oscillating vortices. The double rotor systems experience this same ef-
 297 fect, but are delayed nearly double the distance downstream, and the peak wake
 298 width is reduced. Following the peaks, both wakes dissipate as internal mixing
 299 and momentum transfer with the free stream brings them to a more uniform
 300 velocity and spreads out the deficit effect as can be seen in Figures 8 and 9.

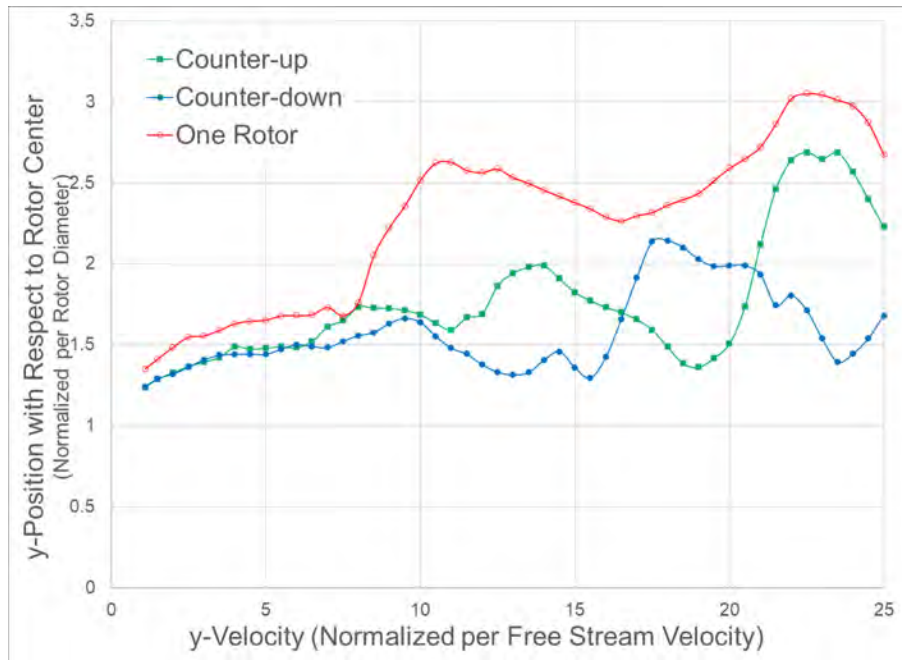


Figure 7: Rotor wake width normalized by the rotor diameter at positions measured downstream from the rotor center. The rotor wake is defined as the distance it takes for the velocity deficit to recover to within 95% of the free stream velocity.

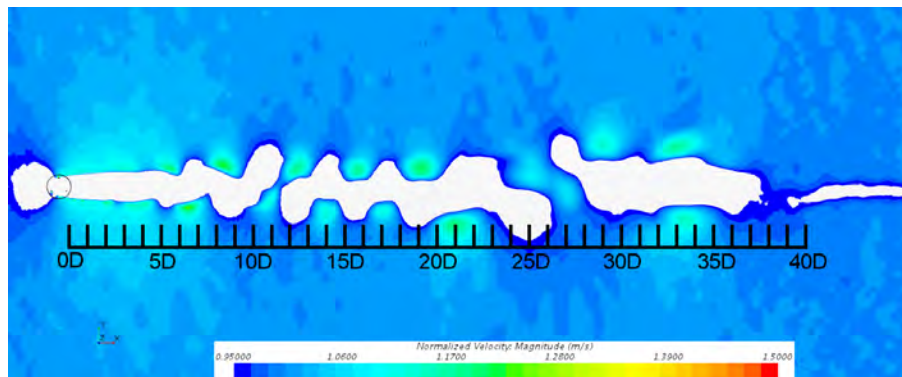


Figure 8: Single rotor wake width based on velocity. Values less than 95% of free stream are shown as white.

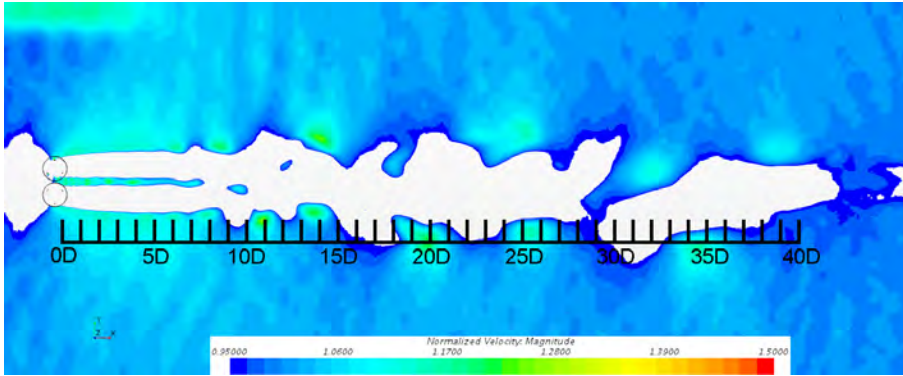


Figure 9: Counter-down double rotor wake width based on velocity. Values less than 95% of free stream are shown as white.

301 The cross-stream distribution of the wake at three downstream locations
 302 is shown in Figure 10 using the (a) streamwise and (b) cross-stream velocity
 303 components. The streamwise velocity distribution shows the expected velocity
 304 deficit immediately downstream of the rotors. In this zone, the velocity deficit
 305 for the double rotor system is both narrower in the y/d direction and shallower
 306 in u/U_∞ direction. This indicates that more energy remains in the direct wake
 307 of the double rotor system as it has a greater total momentum. Additionally, the
 308 streamwise velocity deficit is shifted away from the double rotor system center
 309 so that it is asymmetric about the rotor center. A casual examination might
 310 find it surprising that the double rotor seems to have a smaller total velocity
 311 deficit as this is an indication that less energy has been harvested. In this case,
 312 it is just a further demonstration that more volumetric flow passes through the
 313 rotor center.

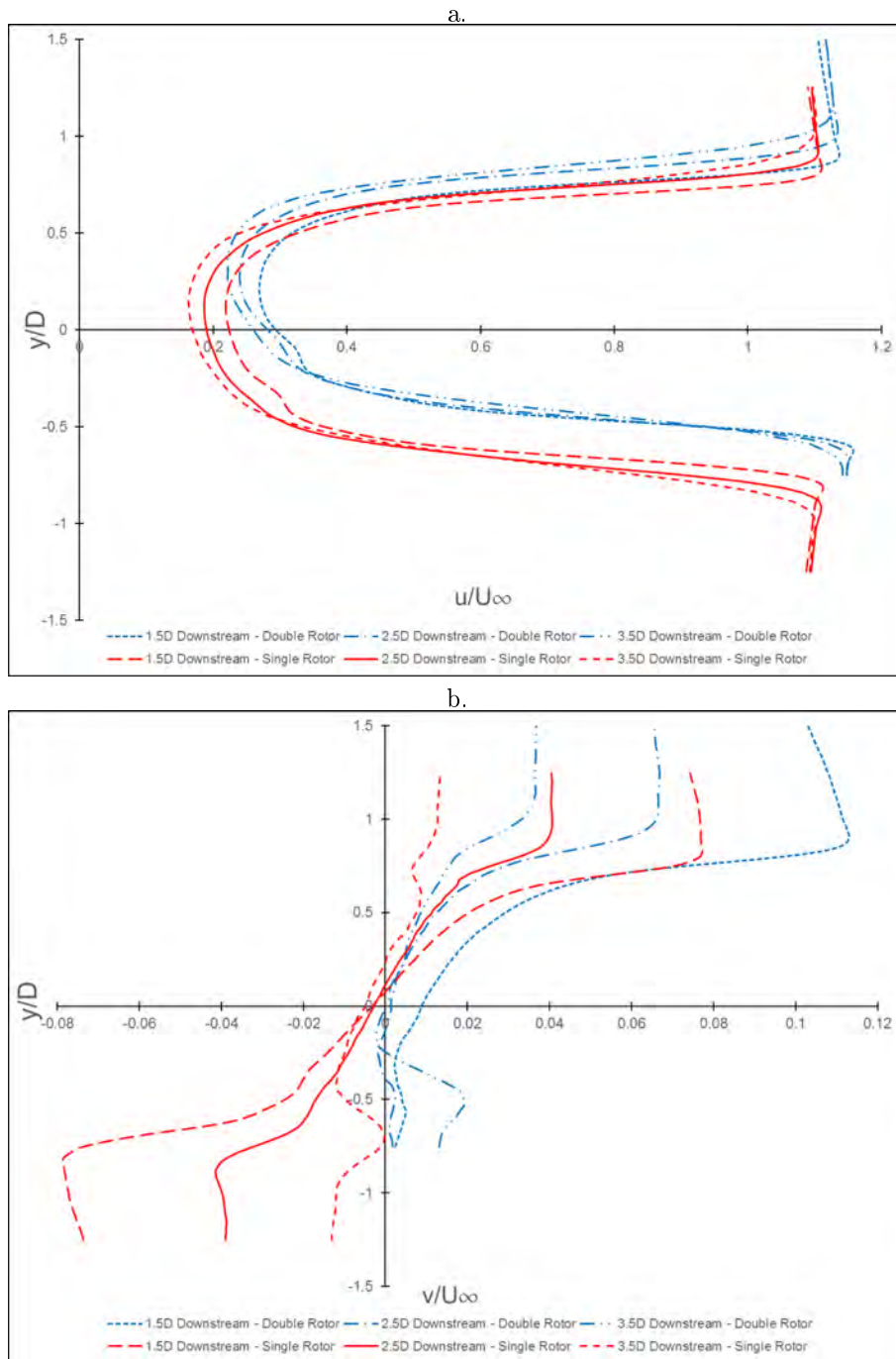


Figure 10: Instantaneous (a) u and (b) v velocities in the rotor wake at three positions downstream of the rotor center versus y -distance from the rotor center. Velocities are non-dimensionalized by the free stream velocity and distances are normalized by the rotor diameter.

314 The last item to note is that the u velocity increases above the free stream
315 value as y/D goes above about 0.75. Since $y/D = 0.5$ marks when the measure-
316 ment position is no longer directly downstream of the rotor, this means that
317 the velocity does not recover to the free stream value until it is well away from
318 the edge of the rotor. Yet, due to bypass, once u/U_∞ reaches parity with the
319 free stream it continues to increase with distance away from the rotor until it
320 reaches about 10% to 15% above free stream. It then begins a slow decrease
321 back down to the free stream condition with further distance from the rotor.
322 Note that on the positive y/D side of the plot, the u/U_∞ for the double rotor
323 system is above the u/U_∞ for the same point in the single rotor system. This is
324 an indication that the double rotor system experiences greater bypass flow away
325 from the center of the two rotor system. The negative y/D side shows that the
326 double rotor has a higher maximum value, but most points experience a lower
327 velocity indicating a lower overall bypass in between the two rotors than the
328 single rotor experiences to a side.

329 The cross-stream velocity distribution shows that very little cross-stream
330 velocity is present in the near field wake. Note that the cross-stream velocity
331 for the two rotor system is very near to zero at the center point between the
332 two rotors ($y/D = -0.75$). This is to be expected, as the u velocities from each
333 rotor will cancel each other out. Outside of the two rotor system, each point
334 in the wake has a higher v -velocity than the corresponding point in the single
335 rotor system.

336 3.3. Volumetric Flow

337 Flow that does not enter the rotor domain cannot be harvested for energy.
338 Correspondingly, it is well known that the blockage effects of wind turbines
339 results in a high pressure upstream that re-directs some incoming wind flow
340 around the outside of the turbine [29, 24]. This is an extension of the well
341 known Betz limit [4]. The Betz-Lanchester analysis enforces the idea that the
342 downstream flow must be reduced in velocity in comparison to the upstream
343 flow. A simple Bernoulli analysis shows that as the streamline approaches the
344 turbine (before energy extraction) the velocity will have to decrease which will
345 have the concurrent effect of increasing the static pressure. This effect can be
346 physically seen in the velocity vector fields discussed in the next section (Figure
347 12), but this section focuses on quantifying the actual volumetric flow entering
348 the rotor domain.

349 The volumetric flow calculations are calculated using the simulation sets
350 with slip boundary conditions so that conservation of mass in the domain is
351 satisfied. Using these parameters, the single rotor pushes 54.1% of the incoming
352 flow (frontal area times average velocity) outside of the rotor. The double rotor
353 systems reduce this loss to an average of 51.0% and 49.1% for the counter-
354 down and counter-up arrangements, respectively (Table 4). This represents a
355 reduction in bypass flow from the single rotor of 5.8% and 9.3%. Not all of this
356 increase in flow will be effectively used for energy harvest as the orientation of
357 the flow passing over the airfoils determines the energy harvest but it does help.
358 Also, it is important to note that the reduction in bypass flow in the double rotor

359 system is entirely due to prevention of bypass flow in between the two rotors. As
 360 noted with the high outside wake velocities in the rotor wake analysis, the bypass
 361 flow to the non-adjacent side of the system actually accounts for a majority of
 362 the total bypass. Using Equation 8, these increases in volumetric flow give
 363 expected power increases of 11.9% and 19.5%. In a general sense, these values
 364 compare favorably to the 10.1% and 13.2% increases found in the simulations
 365 although the discrepancy on the counter-up arrangement reinforces that not all
 366 of the recovered bypass flow is being harnessed by the rotor.

	Non-Adjacent Side Bypass as Fraction of Expected Flow	Total Bypass as Fraction of Expected Flow	Reduction in Total Bypass Compared to Single Rotor
Single Rotor	0.271	0.541	
Counter-Down	0.504	0.510	5.8%
Counter-Up	0.478	0.491	9.3%

Table 4: Average bypass around rotors. Expected flow is calculated as the average velocity over the rotor frontal area.

367 An approximation of the flow passing over the airfoils at different times in
 368 the cycle can be obtained by taking a cycle average of the normalized velocity.
 369 Figure 11 shows the time average of \bar{U}/U_∞ passing through a surface area of
 370 1/10th of a cycle. So, the first point represents the time average of \bar{U}/U_∞
 371 passing through the surface from the zero position down to the 0.1 position.
 372 Each point is represented on the figure at the center point of the section.

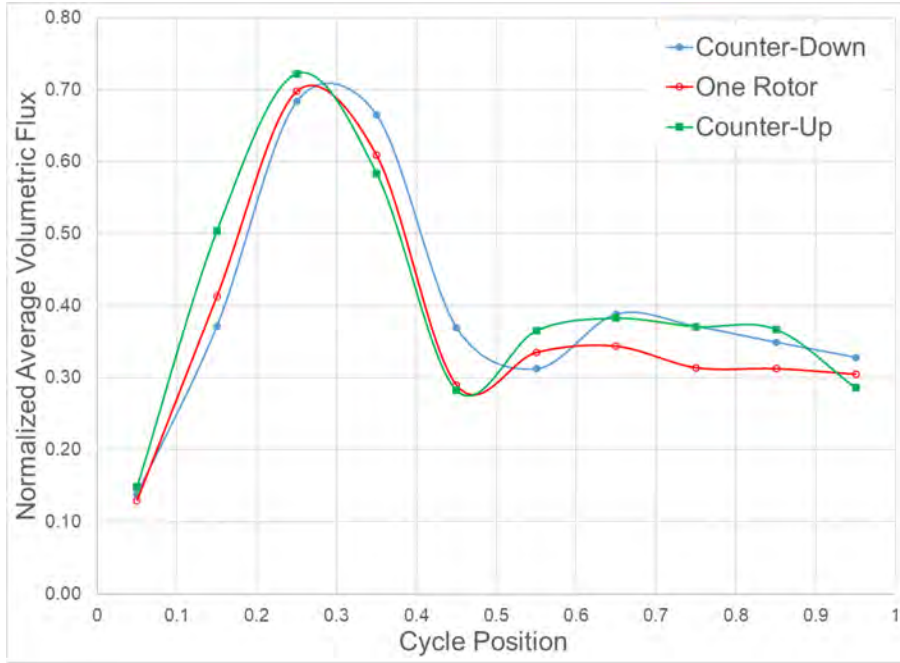


Figure 11: Section surface average of \bar{U}/U_∞ passing through each section of an imaginary cylinder encompassing the path of the airfoils.

373 It is interesting to note the similarity of this plot to the C_P plot in Figure
 374 6. While there are some differences in slope, probably caused by the coarseness
 375 of using 1/10th of the cycle, the overall shapes are quite similar with the effects
 376 of Sections A, B, C, and D being readily identifiable. This emphasizes the
 377 importance of properly channeling the flow into the rotor domain. Any change
 378 in bypass flow can directly impact the rotor output.

379 3.4. Pressure Field and Velocity Vectors

380 The dominating difference between the two rotor system and the single rotor
 381 system is the collision of the cross-stream velocities between the rotors. The
 382 effects of this can be observed by examining the pressure field as the airfoils
 383 approach each other (Figure 12). While the pressure results do show some
 384 artifacts and still suffer from some of the spurious reflections mentioned in the
 385 CFD Setup section, a high pressure unification consistently appears as the two
 386 rotors approach the center as seen in Figures 12 a, c and f. On the single rotor
 387 system, the only high pressure observed is limited to the immediate vicinity of
 388 the airfoil currently in the upstream position.

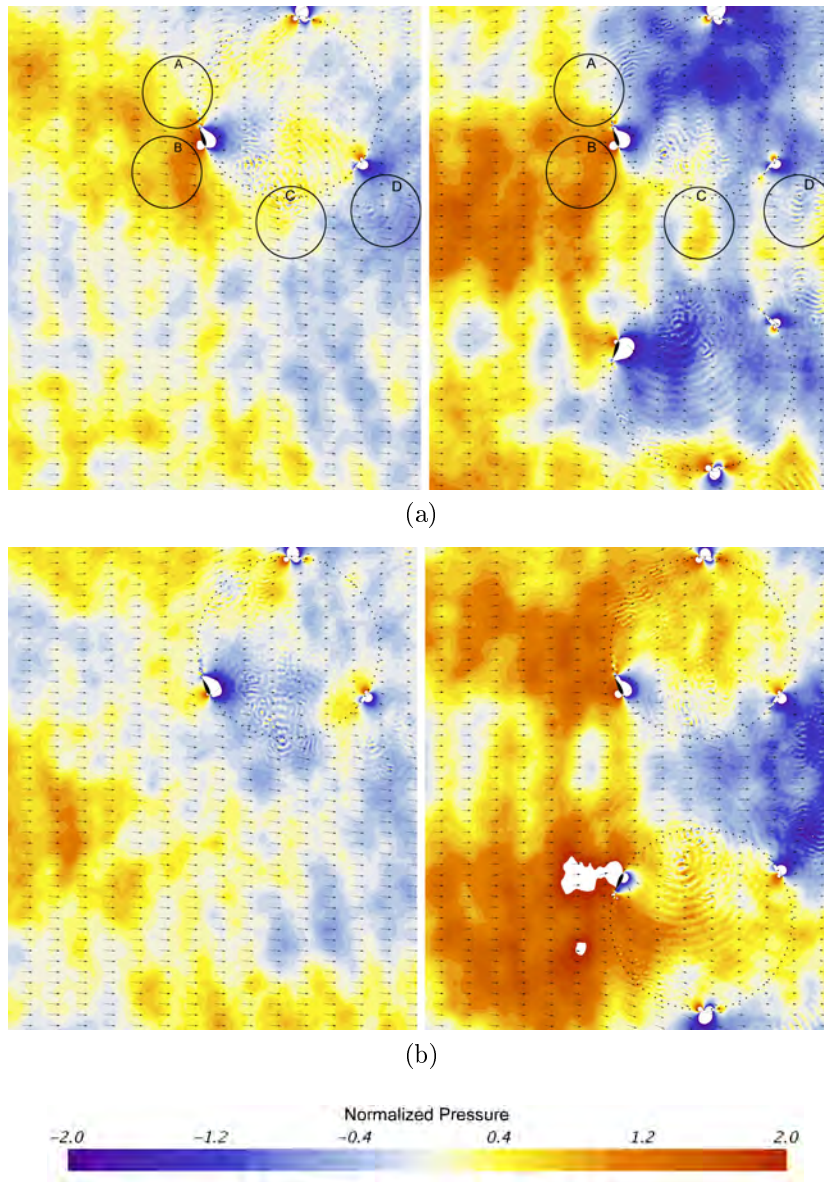
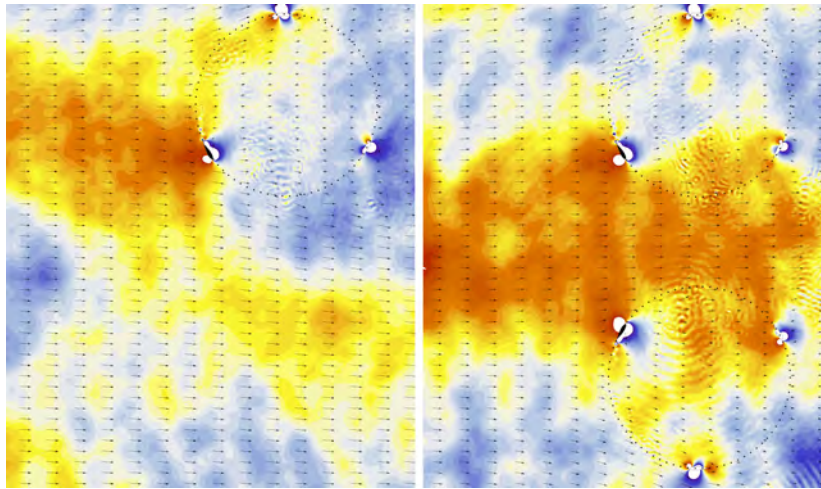
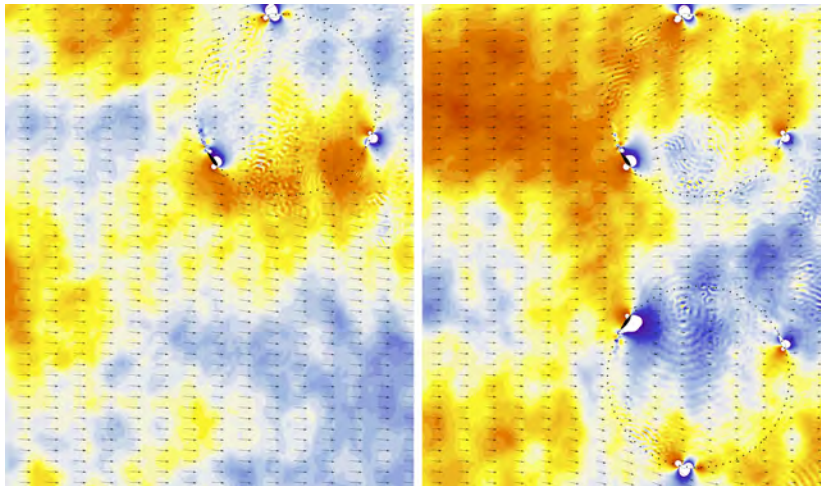


Figure 12: Contours of instantaneous static pressure non-dimensionalized with atmospheric pressure with velocity vectors. The single rotor system is on the left of each figure and the counter-down double rotor system is shown to the right. The airfoils of interest (colored in black) are shown at positions $Z=$: (a) 0.302 (b) 0.318 (c) 0.333 (d) 0.349 (e) 0.365 (f) 0.380 (g) 0.396 (h) 0.411. White demonstrates that the pressure is out of the legend range.



(c)



(d)

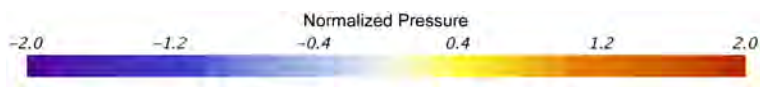
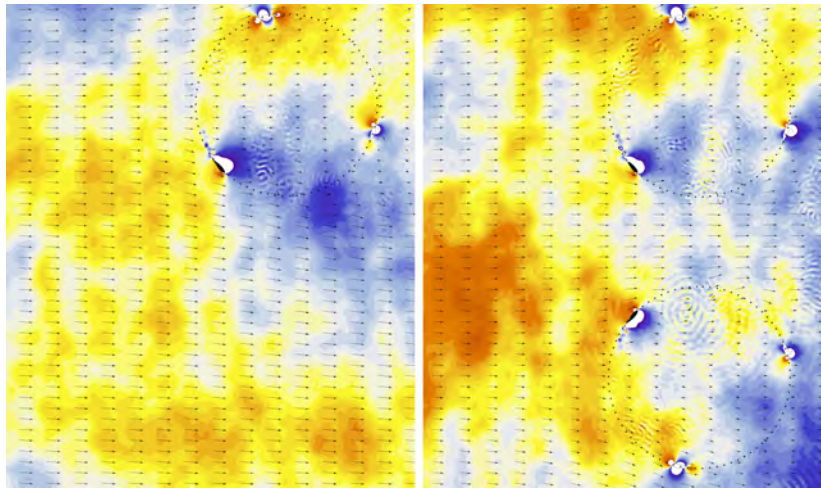
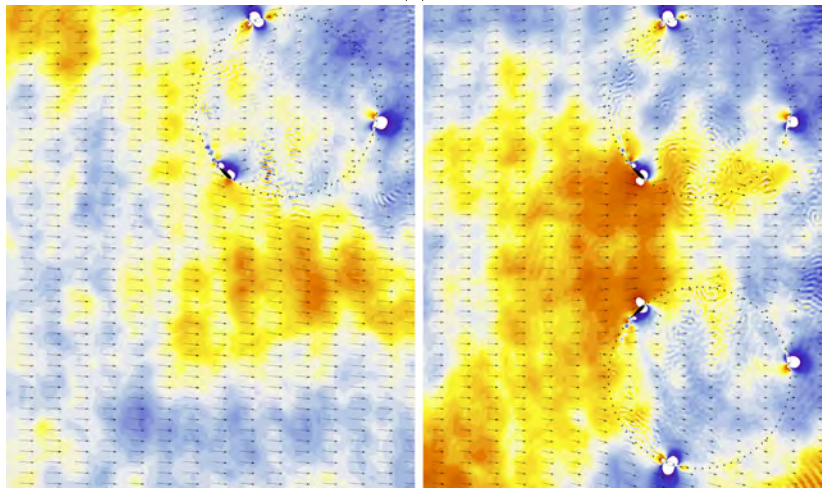


Figure 12: Contours of instantaneous static pressure non-dimensionalized with atmospheric pressure with velocity vectors. The single rotor system is on the left of each figure and the counter-down double rotor system is shown to the right. The airfoils of interest (colored in black) are shown at positions $Z=$: (a) 0.302 (b) 0.318 (c) 0.333 (d) 0.349 (e) 0.365 (f) 0.380 (g) 0.396 (h) 0.411. White demonstrates that the pressure is out of the legend range.

390



(e)



(f)

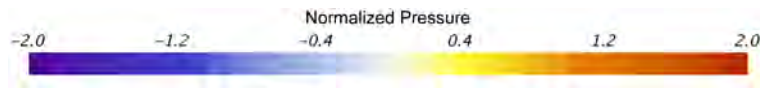


Figure 12: Contours of instantaneous static pressure non-dimensionalized with atmospheric pressure with velocity vectors. The single rotor system is on the left of each figure and the counter-down double rotor system is shown to the right. The airfoils of interest (colored in black) are shown at positions $Z=$: (a) 0.302 (b) 0.318 (c) 0.333 (d) 0.349 (e) 0.365 (f) 0.380 (g) 0.396 (h) 0.411. White demonstrates that the pressure is out of the legend range.

391

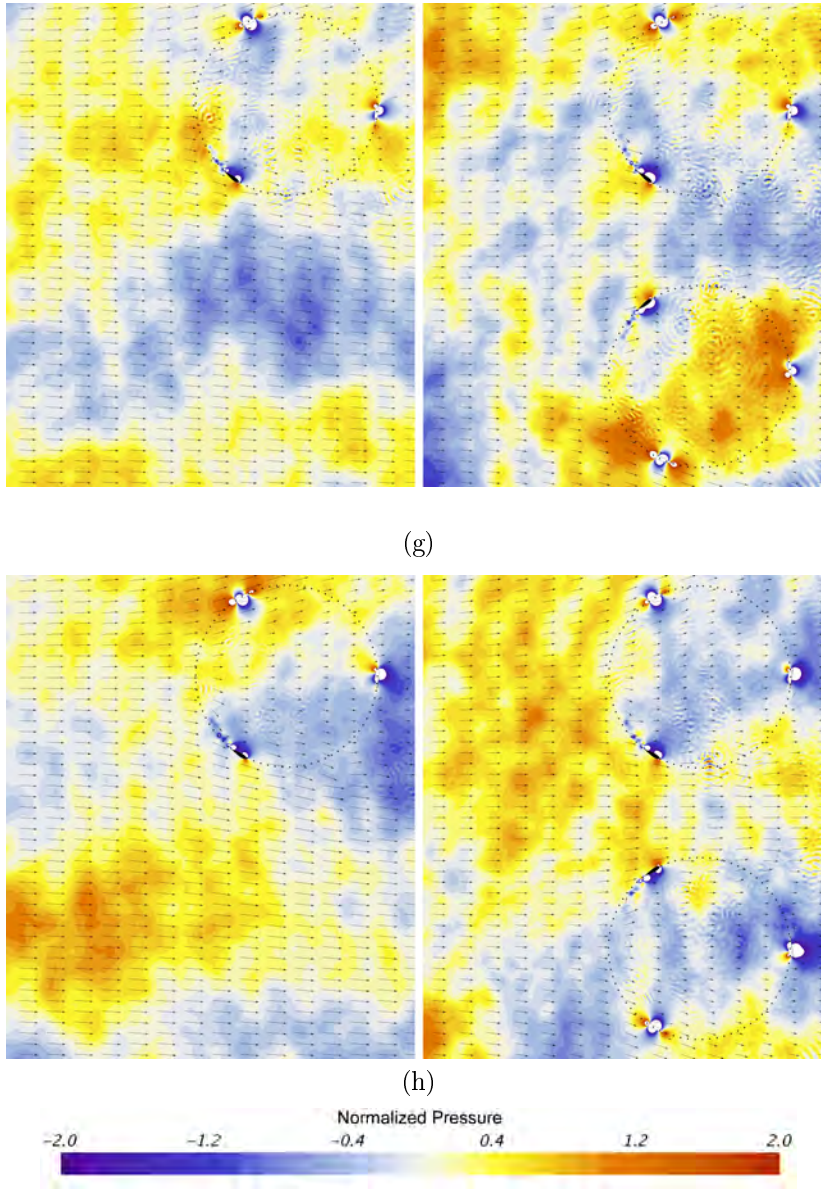


Figure 12: Contours of instantaneous static pressure non-dimensionalized with atmospheric pressure with velocity vectors. The single rotor system is on the left of each figure and the counter-down double rotor system is shown to the right. The airfoils of interest (colored in black) are shown at positions $Z=$: (a) 0.302 (b) 0.318 (c) 0.333 (d) 0.349 (e) 0.365 (f) 0.380 (g) 0.396 (h) 0.411. White demonstrates that the pressure is out of the legend range.

392

393 The most obvious effect of the opposing cross-stream velocities between the
394 two rotors is a straightening of the flow in the gap. This can be readily seen
395 with the vectors in circle C of Figure 12a. Yet, the effect of the correlated high
396 pressure zone can also be seen inside circle A of Figure 12a. The vectors are
397 angled upwards at a slightly greater angle in the double rotor system. This is
398 most likely the cause of the increase in flow lost to the outside. Additionally,
399 the upward flow directly opposes the airfoil motion in $Z = 0.0$ to 0.3 which
400 demonstrates the cause of the drop in the counter-down double rotor C_P for
401 Section A of Figure 6.

402 While the addition of a further upward angle to the vectors can be a negative
403 for circle A, it is clear that it is beneficial in circle B. Instead of the downward
404 angle found in the single rotor system, the upwards pressure creates straight
405 vectors that flow into the optimum area of rotor power generation. This is the
406 cause of the additional volumetric flow shown in Figure 11 from cycle positions
407 0.3 to 0.5 , with a concomitant increase in C_P in Section B (Figure 6).

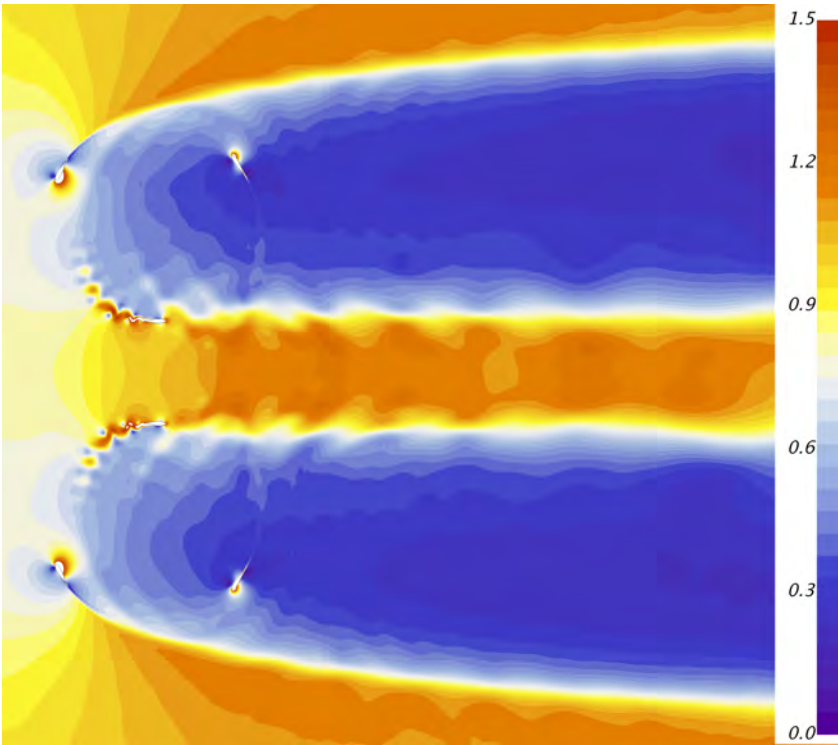
408 With the performance differences of Section A and B explained, scrutiny
409 turns to the drop of double rotor C_P in Section C. Intuitively, this might be
410 unexpected because the double rotor system strengthens the tailwind of the
411 rotor as it progresses from $Z = 0.5$ to 0.6 which reduces the drag experienced.
412 Yet, this overlooks the counter intuitive peculiarity of a lift-based VAWT.

413 Airfoils are normally used to produce lift at very modest angles of attack.
414 Yet, in a lift-based VAWT, flow introduced to the airfoil directly along the
415 chord does not provide torque since it is principally along the axis of the airfoil
416 support. Thus, any moment arm about the center of rotation is very small. To
417 generate substantial torque the lift needs to be perpendicular to the direction of
418 rotation. So, effective lift is only produced when flow impacts the airfoil along
419 the radial direction of the rotor. Figure 12 shows that in the double rotor system
420 the flow is mostly tangential to the airfoil when it is in Section C. In the single
421 rotor system, the flow has a radial component which leads to the single rotor
422 producing more power in this section of the cycle.

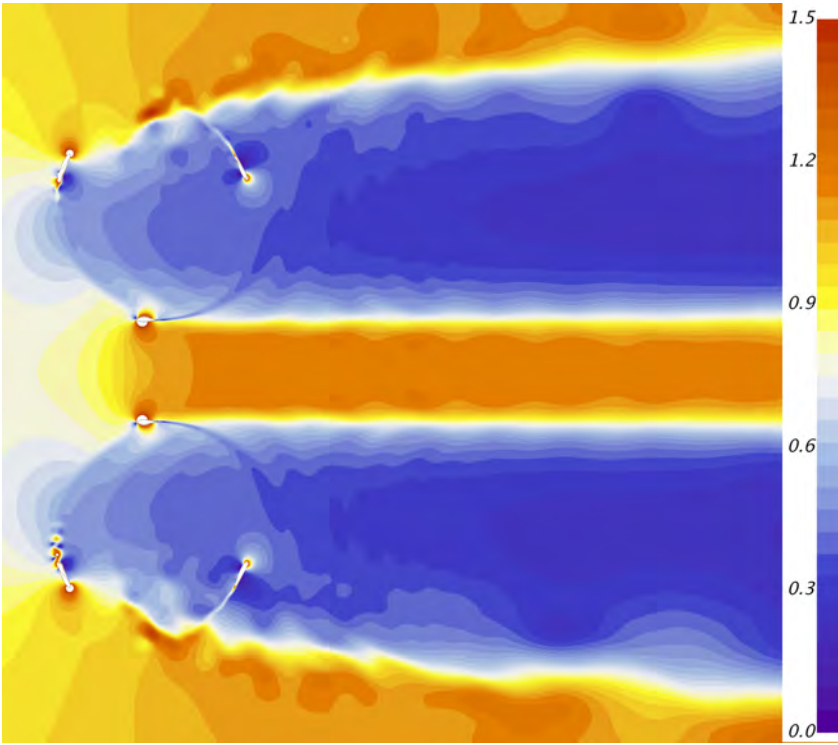
423 Section D composes the entire downstream side of the rotor. The reduction
424 in flow through Section D, as seen by smaller velocity vectors, demonstrates
425 why this section has a lower C_P . Yet, this section does still produce 15% to
426 20% of the total rotor energy. The velocity vectors can be hard to compare
427 in the downstream sections because their magnitudes are so reduced. Yet, the
428 volumetric flow analysis has already shown that more flow passes the down-
429 stream boundary. The result of this additional flow can be seen by looking at
430 the pressure field over the downstream airfoils of Figure 12. The high pressure
431 zone on the inside nose of the double rotor system is quite a bit smaller while
432 the low pressure zone on the outside nose is marginally larger. This results in a
433 large forward torque on the airfoil.

434 *3.5. Velocity Magnitude*

435 Figure 13 shows that the counter-up and counter-down rotors produce in-
436 triguingly different velocity fields. The counter-down rotor airfoils approach the
437 gap between the rotors after coming through the high velocity area in front
438 of the rotor. This means that it is actively shedding vortices. These vortices
439 are convected downstream into the rotor wake where they cause a jagged in-
440 terface between the lower velocity wake region and the high velocity that has
441 passed through the gap. When the counter-up rotor airfoil approaches the gap,
442 it is coming from the downstream side of the rotor and thus has been passing
443 through lower velocity flow. Thus, the wake behind the airfoil is straighter and
444 is not experiencing the vortex shedding seen in the counter-down rotor. This
445 means that it creates a much smoother interface between the rotor wake and
446 gap flow. Conversely, the counter-up system then has a more chaotic rotor wake
447 and free-stream flow interface on the non-adjacent side as it is shedding vortices
448 when it approaches that side.



(a)



(b)

Figure 13: Contours of instantaneous velocity normalized by free stream velocity. (a) counter-down (b) counter-up.

449

450 Additionally, the velocity field in the gap itself is very different between the
 451 two systems. The counter-up system has much slower velocity in the front of the
 452 gap with larger velocity gradients in that region. This leads to a higher pressure
 453 in the gap as shown in Figure 14. It turns out that the air pushed ahead of
 454 the airfoil collides with the incoming free-stream air to create this high pressure
 455 field. A high pressure field in the gap leads to more flow being re-directed away
 456 the gap and back into the rotor domain.

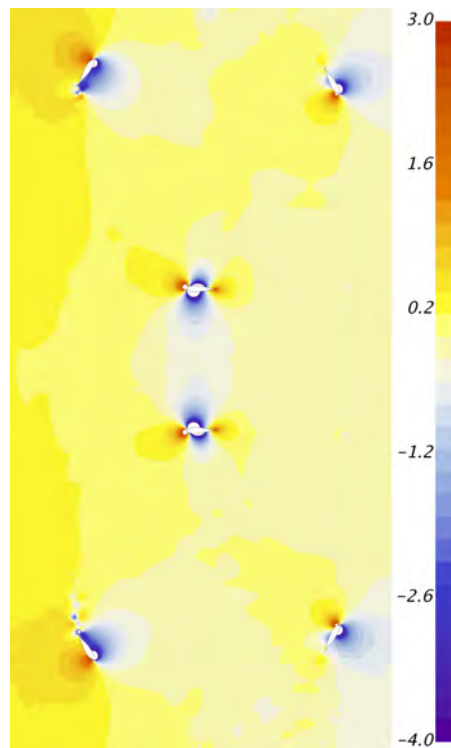


Figure 14: Contours of instantaneous pressure normalized by free stream dynamic pressure.

457

458 Intuitively, the counter-up rotor would be expected to produce less power as
 459 its airfoils progress upstream along the high velocity gap rather than the lower
 460 velocity shielded non-adjacent side like the counter-down rotors. Yet, the drag
 461 on the rotor is more than compensated by the further reduction of bypass flow
 462 caused by the higher gap pressure field.

463 4. Discussion

464 The current study has examined the flow physics behind the individual tur-
 465 bine power increase that occurs when VAWTs are placed in closely spaced arrays.
 466 As derived by Betz, flow going through a turbine will have energy removed re-
 467 sulting in velocity reduction and expansion of the flow [4]. The result of this
 468 is an increase in static pressure upstream of the rotor which causes a portion
 469 of the upstream flow to divert around the rotor. In a single rotor system, this
 470 wind energy is lost downstream. This study has shown that when two VAWTs
 471 are placed in a closely spaced array, the interference of the oppositional cross-
 472 stream velocities between the rotors results in a high pressure field that is now
 473 symmetric about the center gap between the rotors. Flow that would normally
 474 bypass the turbine to that side is now pushed up and away from the gap be-
 475 tween the two rotors. This re-directed flow increases the volume of air entering
 476 the rotor as well as the air bypassing to the opposite side of the turbine. An
 477 examination of Equations 1, 2, and 3 has shown that the increase in volumetric
 478 flow entering the rotor can explain the full power increase over a single rotor
 479 system.

480 An obvious solution to the extra bypass on the side away from the second
 481 rotor might be to put a third, fourth, fifth, etc. rotor in line at the same spacing.
 482 The previously mentioned paper by Zanforlin et al. [28] does show a performance
 483 increase for each turbine when three hydrodynamic turbines are modeled in a
 484 line. The possible pitfall in extending the arrays to larger numbers is that the
 485 total blockage combines to give a large high pressure further upstream of the
 486 turbine. As this high pressure field is extended upstream, the flow going to the
 487 center turbines will become compromised.

488 Additionally, the omnidirectional wind benefit of VAWTs is compromised
 489 further for each additional rotor put into the line. Meaning that performance
 490 may be good with wind directions that are largely perpendicular to the line of
 491 VAWTs, but as the wind angle decreases with respect to that line the output of
 492 the center VAWTs will drop due to blockage by VAWTs upstream in the line.
 493 Thus, while this be a good option to consider for the relatively static direction
 494 of water flows, it may not be appropriate for the mutable nature of wind.

495 While most of the present findings, including percent increase in C_P , changes
 496 to the rotor wake, and velocity increase in the gap between rotors, match up well
 497 with the findings presented by other researchers, one inconsistency should be
 498 noted. The literature on Windspire VAWT C_P simulation results shows a great
 499 degree of variability. The reported single rotor values include 0.24 [28], 0.28 [17],
 500 0.29 [3], and 0.48 [15]. Reported C_P values for double rotor Windspire VAWTs
 501 include 0.27 [28], 0.32 [17], and 0.52 [15]. The results from this study are a
 502 little higher than the average of these values, but are within the reported range.
 503 The differences in these values are not particularly surprising as a variety of
 504 simulation methods, meshes, solvers, and boundary conditions have been used,
 505 but this does provide motivation for further high fidelity studies in the future.

506 5. Conclusion and Future Work

507 Using two-dimensional CFD simulations, this paper reveals the mechanisms
 508 for the C_P increase in double rotor systems previously documented by other
 509 researchers. By building upon the findings of those researchers that the center
 510 velocity straightening and wake width reductions were the likely reason for the
 511 performance improvement, this paper has used the pressure field to demonstrate
 512 how the flow is pushed back into the rotor while quantifying for the first time
 513 that the flow increase is in the range of 16%.

514 The amount of extra flow entering the rotor has been approximated versus
 515 position in the cycle showing that where more flow enters, the C_P is increased.
 516 This establishes a direct correlation between inflow for a certain region with
 517 C_P performance. Each of the discrete sections of the power cycle are analyzed
 518 demonstrating that the performance differences are due to the flow field over
 519 each section. Sections A and C demonstrate a reduced C_P in the counter-
 520 down double rotor system because the flow is straighter and thus generates
 521 less beneficial torque. Sections B and D demonstrate an increased C_P in the
 522 counter-down double rotor system because the flow is stronger, generating more
 523 beneficial torque.

524 These benefits combine together to give a total rotor performance increase in
 525 the range of 10%. For future work, it would be instructive to measure the flow
 526 entering each rotor as the wind direction is varied and compare these results
 527 with the Dabiri [12] measurements of C_P at the corresponding incident angles.
 528 The domain should then be extended to included extra rotors in the line to
 529 again see the impact on entering volumetric flow with respect to wind direction.
 530 This would be an extension of the work others who have looked at the result
 531 of wind farms made of pairs of turbines [1, 6, 7, 19, 27]. Finally, future work
 532 should make the effort to include the hub losses in the simulation.

6. Acknowledgments

This work was completed utilizing the High Performance Computing Center facilities of Oklahoma State University at Stillwater.

7. References

References

- [1] Araya, D.B., Craig, A.E., Kinzel, M., Dabiri, J.O., 2014. Low-order modeling of wind farm aerodynamics using leaky rankine bodies. *Journal of Renewable and Sustainable Energy* 6. doi:10.1063/1.4905127.
- [2] Balduzzi, F., Bianchini, A., Maleci, R., Ferrara, G., Ferrari, L., 2016. Critical issues in the CFD simulation of darrieus wind turbines. *Renewable Energy* 85, 419–435. doi:10.1016/j.renene.2015.06.048.

- [3] Bazilevs, Y., Korobenko, A., Deng, X., Yan, J., Kinzel, M., Dabiri, J., 2014. Fluid-structure interaction modeling of vertical-axis wind turbines. *Journal of Applied Mechanics* 81. doi:10.1115/1.4027466.
- [4] Betz, A., 1966. Introduction to the theory of flow machines. Pergamon.
- [5] Bianchini, A., Balduzzi, F., Bachant, P., Ferrara, G., Ferrari, L., 2017. Effectiveness of two-dimensional CFD simulations for darrieus vawts: a combined numerical and experimental assessment. *Energy conversion and management* 136, 318–328. doi:10.1016/j.enconman.2017.01.026.
- [6] Bremseth, J., Duraisamy, K., 2016. Computational analysis of vertical axis wind turbine arrays. *Theoretical and Computational Fluid Dynamics* 30, 387–401.
- [7] Brownstein, I.D., Kinzel, M., Dabiri, J.O., 2016. Performance enhancement of downstream vertical-axis wind turbines. *Journal of Renewable and Sustainable Energy* 8. doi:10.1063/1.4964311.
- [8] Castelli, M.R., Ardizzon, G., Battisti, L., Benini, E., Pavesi, G., 2010. Modeling strategy and numerical validation for a darrieus vertical axis micro-wind turbine, in: *ASME 2010 International Mechanical Engineering Congress and Exposition, American Society of Mechanical Engineers*. pp. 409–418. doi:10.1115/IMECE2010-39548.
- [9] Chen, W.H., Chen, C.Y., Huang, C.Y., Hwang, C.J., 2017. Power output analysis and optimization of two straight-bladed vertical-axis wind turbines. *Applied Energy* 185, 223–232. doi:10.1016/j.apenergy.2016.10.076.
- [10] Craig, A., Dabiri, J.O., 2015. V-shaped arrangements of turbines. US Patent 9,175,669.
- [11] Craig, A.E., Dabiri, J.O., Koseff, J.R., 2016. Flow kinematics in variable-height rotating cylinder arrays. *Journal of Fluids Engineering* 138. doi:10.1115/1.4033676.
- [12] Dabiri, J.O., 2011. Potential order-of-magnitude enhancement of wind farm power density via counter-rotating vertical-axis wind turbine arrays. *Journal of Renewable and Sustainable Energy* 3. URL: <http://scitation.aip.org/content/aip/journal/jrse/3/4/10.1063/1.3608170>, doi:10.1063/1.3608170.
- [13] Dabiri, J.O., Greer, J.R., Koseff, J.R., Moin, P., Peng, J., 2015. A new approach to wind energy: opportunities and challenges, in: *AIP Conference Proceedings, AIP*. pp. 51–57. doi:10.1063/1.4916168.
- [14] Daróczy, L., Janiga, G., Petrasch, K., Webner, M., Thévenin, D., 2015. Comparative analysis of turbulence models for the aerodynamic simulation of H-darrieus rotors. *Energy* 90, 680–690. doi:10.1016/j.energy.2015.07.102.

- [15] De Tavernier, D., Simao Ferreira, C., Li, A., Paulsen, U.S., Madsen, H.A., 2018. Vawt in double-rotor configuration: the effect on airfoil design, in: 2018 Wind Energy Symposium.
- [16] Ghasemian, M., Ashrafi, Z.N., Sedaghat, A., 2017. A review on computational fluid dynamic simulation techniques for darrieus vertical axis wind turbines. *Energy Conversion and Management* 149, 87 – 100. URL: <http://www.sciencedirect.com/science/article/pii/S0196890417306519>, doi:<https://doi.org/10.1016/j.enconman.2017.07.016>.
- [17] Giorgetti, S., Pellegrini, G., Zanforlin, S., 2015. CFD investigation on the aerodynamic interferences between medium-solidity darrieus vertical axis wind turbines. *Energy Procedia* 81, 227–239. doi:[10.1016/j.egypro.2015.12.089](https://doi.org/10.1016/j.egypro.2015.12.089).
- [18] Huskey, A., Bowen, A., Jager, D., 2009. Wind Turbine Generator System Power Performance Test Report for the Mariah Windspire 1-kW Wind Turbine. Technical Report. National Renewable Energy Laboratory (NREL), Golden, CO.
- [19] Kinzel, M., Mulligan, Q., Dabiri, J., 2012. Energy exchange in an array of vertical-axis wind turbines. *Journal of Turbulence* 13, 1–13. URL: <http://www.tandfonline.com/doi/abs/10.1080/14685248.2012.712698>.
- [20] Laino, D., Davis, D., 2013. Power Performance Test Report for the Windspire. Technical Report. Windward Engineering, LLC.
- [21] Lam, H., Peng, H., 2016. Study of wake characteristics of a vertical axis wind turbine by two- and three-dimensional computational fluid dynamics simulations. *Renewable Energy* 90, 386 – 398. URL: <http://www.sciencedirect.com/science/article/pii/S0960148116300118>, doi:<https://doi.org/10.1016/j.renene.2016.01.011>.
- [22] Lanzafame, R., Mauro, S., Messina, M., 2014. 2d CFD modeling of darrieus wind turbines using a transition turbulence model. *Energy Procedia* 45, 131–140.
- [23] Rezaeiha, A., Montazeri, H., Blocken, B., 2018. Towards accurate CFD simulations of vertical axis wind turbines at different tip speed ratios and solidities: Guidelines for azimuthal increment, domain size and convergence. *Energy Conversion and Management* 156, 301 – 316. URL: <http://www.sciencedirect.com/science/article/pii/S0196890417310786>, doi:<https://doi.org/10.1016/j.enconman.2017.11.026>.
- [24] Schatzle, P., Klimas, P.C., Spahr, H., 1981. Aerodynamic interference between two darrieus wind turbines. *Journal of Energy* 5, 84–88.
- [25] Siemens, 2016. Star-CCM+.

- [26] Sinclair, K., Bowen, A., 2008. Testing small wind turbines at the national renewable energy laboratory: Nrel/cp-500-43452, in: *Wind Power*.
- [27] Whittlesey, R.W., Liska, S., Dabiri, J.O., 2010. Fish schooling as a basis for vertical axis wind turbine farm design. *Bioinspiration & Biomimetics* 5. doi:10.1088/1748-3182/5/3/035005.
- [28] Zanforlin, S., Nishino, T., 2016. Fluid dynamic mechanisms of enhanced power generation by closely spaced vertical axis wind turbines. *Renewable Energy* 99, 1213–1226. doi:10.1016/j.renene.2016.08.015.
- [29] Zhang, B., Song, B., Mao, Z., Tian, W., 2017. A novel wake energy reuse method to optimize the layout for savonius-type vertical axis wind turbines. *Energy* 121, 341–355. doi:10.1016/j.energy.2017.01.004.